Research Square

Preprints are preliminary reports that have not undergone peer review.
They should not be considered conclusive, used to inform clinical practice,
or referenced by the media as validated information.

A Reduced Postsynaptic Conductance Model of Complement-Associated Electrical Perturbation at the Neuromuscular Junction

Kevin Thorsen Baird

kbaird@bairdstrategic.com

The C4 Institute, Baird Research & Strategic Sciences, LLC

Research Article

Keywords:

Posted Date: November 16th, 2026

DOI: https://doi.org/10.21203/rs.3.rs-11517246/v1

License: This work is licensed under a Creative Commons Attribution 4.0 International License.
Read Full License

Additional Declarations: Competing interest reported. Kevin Thorsen Baird discloses a U.S. provisional patent application (Application No. 64/100,482), assigned to Baird Research & Strategic Sciences, LLC, concerning bioelectric boundary-modulation concepts and computational modeling frameworks related to this work. Kevin Thorsen Baird is the Principal Investigator at The C4 Institute, Baird Research & Strategic Sciences, LLC.

A Reduced Postsynaptic Conductance Model of Complement-Associated Electrical Perturbation at the Neuromuscular Junction

Kevin Thorsen Baird*

The C4 Institute, Baird Research & Strategic Sciences, LLC, Fort Myers, FL 33907, USA

Abstract

The neuromuscular junction is a specialized bioelectrical interface governed by membrane conductances. In antibody-mediated disorders such as myasthenia gravis, complement-dependent injury disrupts this interface, but the electrical consequences of effective membrane-attack-complex-associated conductance remain incompletely defined. We developed a reduced, capacitance-based postsynaptic membrane model to assess how a time-dependent effective membrane-attack-complex-associated specific conductance changes membrane voltage and local specific input resistance. The model was formulated per unit membrane area and integrated with an adaptive Runge–Kutta 4(5) method. A planar-bilayer C5b-9 conductance measurement and structural pore characterizations were used as conceptual priors; effective conductance, reversal potential, onset, duration, and repair were sensitivity variables. Under an illustrative parameter set, effective conductances of 1.5 and 5.0 mS cm-2 shifted the conductance-weighted steady voltage from -85 mV to approximately -28.8 and -16.8 mV and reduced local specific input resistance from 2.0 to 0.50 and 0.18 k cm2. A phenomenological 90% reduction in effective conductance produced partial, not complete, voltage recovery. A resting transmembrane voltage corresponds to a membrane-scale field of order 107 V m-1 under a uniform-field approximation. Whether complement-associated electrical perturbation changes the local field or conformational state of acetylcholine receptors remains untested. Accordingly, the model defines conditional receptor-coupling analyses and falsifiable electrophysiological and receptor-state

*Corresponding author: Kevin Thorsen Baird, The C4 Institute, Baird Research & Strategic Sciences, LLC, Fort Myers, FL 33907, USA. ORCID: 0009-0001-7938-446X. E-mail: kbaird@bairdstrategic.com

experiments. Poloxamer 188 is considered only as a possible experimental comparator, not as a membrane-attack-complex sealant or therapeutic intervention for myasthenia gravis.

Keywords: Neuromuscular junction · Membrane conductance · Membrane attack complex · Myasthenia gravis · Bioelectricity · Computational biophysics

1 Introduction

Biological membranes and specialized synaptic interfaces rely on tightly regulated ionic conductances and transmembrane electric fields to maintain physiological excitability. To make the biophysical problem accessible across disciplines, we first summarize the fundamental physical mechanism addressed in this study: when pore-forming protein complexes insert into an excitable cell membrane, they introduce a parallel, non-selective electrical conductance that shunts the baseline membrane resistance and drives the transmembrane potential toward the pore reversal potential. In acetylcholine-receptor (AChR)-antibody-positive myasthenia gravis (Gilhus, 2016), complement-fixing autoantibodies activate the classical complement cascade at the postsynaptic motor endplate (Howard, 2018). The terminal complement pathway results in the assembly and deposition of the membrane attack complex (MAC, C5b-9) at the neuromuscular junction (Sahashi et al., 1980; Mozrzymas et al., 1993; Huijbers et al., 2022). Structural and biophysical investigations have resolved the architecture of the MAC as a split-washer transmembrane -barrel pore by cryo-electron microscopy (cryo-EM) (Menny et al., 2018) and characterized its single-molecule assembly kinetics by rapid atomic-force microscopy (Parsons et al., 2019), demonstrating that terminal complement complexes and incomplete intermediates perturb local lipid-bilayer integrity. Concurrently, physiological and structural studies of synaptic transmission and nicotinic receptors have clarified how postsynaptic junctional-fold geometry, receptor clustering, and high-resolution receptor conformational states govern endplate current generation and the neuromuscular safety factor (Wood and Slater, 2001; Song and Corry, 2009; Noviello et al., 2021). While MAC-dependent ultrastructural damage and AChR loss are established mechanisms of synaptic failure, the explicit quantitative electrical consequences of parallel, complement-associated membrane conductance on the local postsynaptic membrane potential and input impedance have not been fully integrated into reduced biophysical frameworks.

Using a computational membrane-modeling approach, we examine whether a

localized effective complement-associated conductance can alter reduced postsynaptic electrical variables and, under an explicitly conditional field-coupling module, motivate testable hypotheses concerning AChR reporter-state behavior and epitope accessibility (Fig. 1).

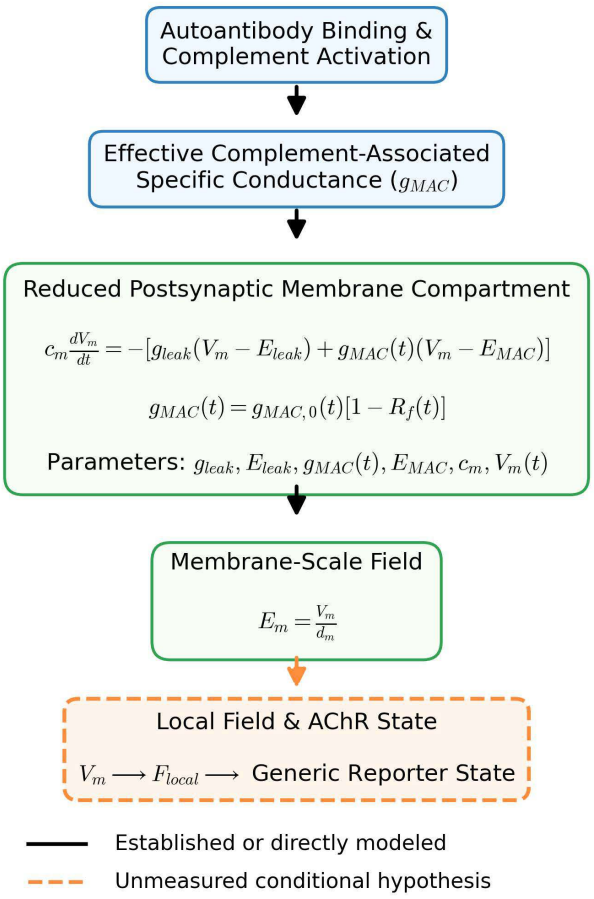


Figure 1: **Biophysical framework and evidence hierarchy.** (**a**) Established evidence in AChR-antibody-positive MG: complement-fixing autoantibodies can activate terminal complement, and C9 immunoreactivity consistent with terminal-complement/MAC deposition has been observed at damaged human motor endplates (Howard, 2018; Huijbers et al., 2022; Sahashi et al., 1980). (**b**) Reduced-model component: a local postsynaptic electrical compartment is represented as an equivalent RC system with gleak, gMAC(t), and cm. (**c**) Conditional hypothesis: receptor-local field coupling and a reporter-state response require direct experimental validation. A generic repair factor, Rf(t), reduces the effective conductance in model scenarios only.

The clinical relevance of terminal complement in a defined subset of myasthenia gravis is supported by randomized trials of C5 inhibition in adults with anti-AChR-antibody-positive generalized disease (Howard et al., 2017; Vu et al., 2022). These studies support terminal complement as a therapeutic target in that population, but they do not test the electrical, local-field, receptor-state, or membrane-repair mechanisms modeled here.

2 Methods and Model Formulation

2.1 Reduced postsynaptic electrical compartment

The model defines a reduced local electrical compartment of the postsynaptic membrane modeled as an equivalent RC circuit per unit area. The temporal evolution of the local transmembrane voltage, Vm(t), is governed by:

$$c_m \frac{dV_m}{dt} = -\left[I_{\text{leak}}(V_m) + I_{\text{MAC}}(V_m, t)\right] \tag{1}$$

where cm is the specific membrane capacitance, Ileak is the specific passive leak current, and IMAC is the specific current resulting from the effective time-dependent complement-associated conductance. The currents are modeled using linear driving forces:

$$I_{\text{leak}}(V_m) = g_{\text{leak}}(V_m - E_{\text{leak}}) \tag{2}$$

$$I_{\text{MAC}}(V_m, t) = g_{\text{MAC}}(t)(V_m - E_{\text{MAC}}) \tag{3}$$

where gleak and Eleak are the baseline passive leak specific conductance and reversal potential, respectively.

For intervals in which the conductances are constant, the local membrane time constant was calculated as:

$$\tau_m = \frac{c_m}{g_{\text{leak}} + g_{\text{MAC}}}. \tag{4}$$

The modeled local specific input resistance was calculated as:

$$R_{\text{in,specific}}(t) = \frac{1}{g_{\text{leak}} + g_{\text{MAC}}(t)}. \tag{5}$$

2.2 Parameterization and conductance scenarios

The model was evaluated across sensitivity ranges because aggregate effective conductance and lesion duration at human motor endplates are unknown. Foundational single-channel C5b-9 planar-bilayer measurements (Benz et al., 1986) alongside cryo-EM structural reconstructions (Menny et al., 2018) and rapid atomic-force microscopy assembly kinetics (Parsons et al., 2019) serve as conceptual priors indicating that terminal complement insertion introduces heterogeneous, non-selective transmembrane conductive pathways. The nominal specific membrane capacitance of $1.0\ \mu$F cm^{-2}

was used as a generic membrane-model prior to set the electrical time scale and was not intended as a direct measurement of the folded human postsynaptic membrane. Table 1 summarizes the nominal electrical and repair parameters and evaluated sensitivity ranges.

Complement attack on nucleated cells can produce sublytic injury and trigger cellular resistance and recovery processes, including removal or repair of terminal-complement lesions (Morgan, 1989; Okamoto et al., 2000). These biological responses are not explicitly represented in the reduced model; instead, their possible net electrical consequence is represented phenomenologically through gMAC(t) and Rf(t).

The imposed pre-repair effective specific conductance waveform, gMAC,0(t), was defined as:

$$g_{\mathrm{MAC},0}(t) = \begin{cases} 0, & t < t_{\mathrm{onset}}, \\ g_{\mathrm{MAC},0}, & t_{\mathrm{onset}} \le t < t_{\mathrm{onset}} + T_{\mathrm{lesion}}, \\ 0, & t \ge t_{\mathrm{onset}} + T_{\mathrm{lesion}}. \end{cases} \tag{6}$$

In simulations without a repair perturbation, gMAC(t)=gMAC,0(t). In repair simulations, the conductance entering Eq. 1 is modified according to Eq. 7. For the persistent-conductance trajectories, Tlesion was set greater than the simulation duration, such that gMAC,0(t) remained constant after tonset throughout the plotted interval. Finite-duration pulses were used only for the transient sensitivity scenarios.

2.3 Generic membrane-repair perturbation

We modeled a generic time-dependent reduction in effective pathological conductance, representing an experimental membrane-repair perturbation, through a generalized repair factor Rf(t). In the generic repair scenario, Rf(t)=0 before trepair=50 ms and Rf(t)=0.90 thereafter.

The effective conductance during the repair scenario was defined as:

$$g_{\mathrm{MAC}}(t) = g_{\mathrm{MAC},0}(t)\,[1 - R_f(t)]\,, \qquad 0 \le R_f(t) \le 1. \tag{7}$$

The repair factor is a phenomenological intervention variable. It does not imply physical occlusion of a C5b-9 pore, altered membrane-attack complex assembly, or a therapeutic effect of any specific compound.

Table 1: Nominal parameters and sensitivity variables of the reduced postsynaptic conductance and repair model. Values are illustrative modeling inputs, not direct measurements at human motor endplates unless otherwise stated.

Parameter	**Symbol**	**Nominal / range**	**Interpretation**
Resting membrane voltage	Vrest	-85 mV	Illustrative baseline postsynaptic state.
Leak reversal potential	Eleak	-85 mV	Set equal to Vrest in nominal simulations.
Leak specific conductance	gleak	0.5 mS cm-2	Baseline model conductance density.
Specific membrane capacitance	cm	$1.0\ \mu$F cm^{-2}	Illustrative generic membrane prior.
Effective lesion onset time	tonset	10 ms (0 ms in verification)	Onset of the effective-conductance waveform.
Effective lesion conductance	gMAC,0	0–10 mS cm-2	Sensitivity variable (200-point grid); not a direct measurement of MAC density.
Effective lesion reversal potential	EMAC	-10 mV nominal (-30 to +10 mV range)	Sensitivity variable evaluated across -30 to +10 mV (200-point grid) and discrete curves at -20,-10,0 mV.
Effective lesion duration	Tlesion	2–40 ms (trajectories), 0.01–2.0 ms (grid), or >Tsim (step)	Duration of the imposed waveform; persistent-step simulations use Tlesion>Tsim.
Simulation duration	Tsim	100–200 ms	Total integration interval for each trajectory.
Repair onset time	trepair	50 ms	Illustrative onset of the phenomenological repair factor.
Repair factor	Rf	0–1; 0.90 nominal	Fractional reduction in the effective conductance (200-point grid).

2.4 Membrane-scale and conditional reporter-state field model

A nominal transmembrane voltage of -85 mV across an assumed 5 nm membrane corresponds to the signed membrane-scale field proxy Em=Vm/dm-17.0 MV m-1 (magnitude 1.7107 V m-1). This estimate is not a measurement of the local field at an AChR residue, interfacial water molecule, or reporter probe. Local fields depend on atomic charge distributions, hydration, protein structure, and dielectric heterogeneity (Fried and Boxer, 2015; Song and Corry, 2009; Noviello et al., 2021). We link the membrane-scale voltage to an independent generic conformational reporter via a conditional local-field shift:

$$\vec{F}_{\text{local}} = \vec{F}_{\text{local},0} + \alpha_F \left(\frac{V_m - V_{\text{ref}}}{d_m} \right) \hat{n} + \Delta \vec{F}_{\text{independent}}, \tag{8}$$

where Flocal,0 is an unspecified reference local field, Vref is the reference membrane voltage, F is a dimensionless conditional coupling parameter, n is the unit normal convention aligned with the signed scalar proxy Vm/dm, and Findependent is an independent phenomenological local-field perturbation. Neither local-field term is measured or derived from the membrane model.

For the conditional two-state sensitivity analysis, we set:

$$\Delta G_{\text{reporter}}(\vec{F}_{\text{local}}) = \Delta G_{\text{reporter},0} - \Delta \vec{\mu}_{\text{eff}} \cdot \left[\vec{F}_{\text{local}} - \vec{F}_{\text{local},0} \right], \tag{9}$$

where Greporter,0 is the reference free-energy difference at Vref and eff is the effective dipole-moment difference projected along n. In the numerical sensitivity sweeps (Table 2), we evaluated Vm across a 200-point grid spanning -100 to +20 mV and F across a 200-point grid spanning 0.0 to 3.0, with Vref=0 mV and Findependent=0, yielding the scalar local-field shift Flocal=F(Vm/dm). To evaluate energetic and conformational state sensitivity in dimensionless thermal-energy units (kBT), Eq. 9 was parameterized as:

$$\frac{\Delta G_{\text{reporter}}(V_m)}{k_B T} = \frac{\Delta G_{\text{reporter},0}}{k_B T} - \kappa V_m, \tag{10}$$

where =(effF)/(dmkBT) is the composite voltage-to-energy coupling sensitivity parameter evaluated at 0.0,0.02,0.05,0.10 mV-1. The reference dimensionless free-energy gap at Vref=0 mV was set to 2.0. The field-mapping analysis varied F, whereas the normalized energy and probability analyses varied the composite parameter ; these were illustrative sensitivity analyses rather than independently calibrated receptor

parameters. The conditional probability of exposing this reporter state is:

$$P_{\text{reporter}+} = \frac{1}{1 + \exp\left(\Delta G_{\text{reporter}}/k_B T\right)}. \tag{11}$$

Table 2: Parameters and evaluated grids of the conditional local-field and generic reporter-state sensitivity module.

Parameter	**Symbol**	**Nominal / range**	**Interpretation**
Membrane thickness	dm	5 nm nominal	Input to the uniform membrane-scale field proxy.
Evaluated voltage grid	Vm	-100 to +20 mV	200-point transmembrane voltage grid for conditional field analysis.
Reference voltage	Vref	0 mV	Reference transmembrane potential at which Flocal=0 and Greporter=Greporter,0.
Local field-coupling parameter	F	0.0–3.0	Dimensionless conditional field-coupling sensitivity input (200-point grid).
Independent field perturbation	Findependent	0 MV m-1	Set to zero in baseline voltage-coupled sensitivity sweeps.
Reference reporter energy gap	Greporter,0/(kBT)	2.0 (dimensionless)	Reference thermal-energy-normalized free-energy gap at Vref=0 mV.
Composite voltage–energy coupling		0.0,0.02,0.05,0.10 mV-1	Composite sensitivity parameter defined as =(effF)/(dmkBT).

2.5 Numerical integration and analytical verification

The dynamical membrane equation was integrated in Python 3.10 using SciPy's adaptive Dormand–Prince Runge–Kutta 4(5) solver (`scipy.integrate.solve_ivp`, method = `RK45`). Nominal trajectory simulations used relative and absolute tolerances of 10-6

and 10-8, respectively, over a 1200-point evaluation grid spanning t=0 to 100 ms (1000-point grid for the 2,10,40 ms transient-pulse trajectories). All trajectories were initialized at Vm(0)=Vrest=-85 mV. In nominal step-waveform trajectory simulations, tonset=10 ms; before onset, gMAC(t)=0 and Eleak=Vrest, such that the model remained at the baseline steady state. Peak voltages for the pulse-duration contour (Tlesion=0.01–2.0 ms) were calculated from the constant-conductance analytical RC charging solution evaluated at pulse termination, Vpeak=V+(Vrest-V)(-Tlesion/m). In the constant-conductance verification and tolerance-convergence analyses, constant gMAC values were applied starting at t=0 ms and integrated to Tsim=200 ms across relative tolerances spanning 10-2 to 10-13 (with absolute tolerance scaled as $10^{-2} \times$ rtol). Large language models (Google Gemini and QuillBot AI) were used during manuscript preparation for language editing, organizational drafting, and software-formatting suggestions, with all mathematical formulations, code execution, and numerical outputs independently verified by the author (see Statements and Declarations).

For constant-conductance scenarios, the numerical steady-state voltage was compared against the analytical limit:

$$V_\infty = \frac{g_{\text{leak}} E_{\text{leak}} + g_{\text{MAC}} E_{\text{MAC}}}{g_{\text{leak}} + g_{\text{MAC}}}. \tag{12}$$

3 Results

3.1 Voltage, input-resistance, and generic repair trajectories

Numerical integration yields the modeled local postsynaptic voltage and specific input-resistance responses to the imposed effective conductance waveform (Fig. 2a–c). Under baseline parameters (gleak=0.5 mS cm-2, Vrest=-85 mV), the modeled onset of an effective complement-associated specific conductance at tonset=10 ms produced a rapid depolarization trajectory on the timescale specified by the assumed capacitance and conductance values (Fig. 2a). Under the illustrative higher-conductance scenario (gMAC=5.0 mS cm-2 and EMAC=-10 mV), the membrane voltage approached the conductance-weighted steady state (V-16.8 mV). Under the illustrative lower-conductance scenario (gMAC=1.5 mS cm-2), the model approached V-28.8 mV.

The insertion of parallel non-selective conductance pathways substantially reduced local specific input resistance (Rin,specific) calculated via Eq. 5 (Fig. 2b). For the 1.5 and 5.0 mS cm-2 conductance scenarios, modeled local specific input resistance declined from 2.0 k cm2 at baseline to 0.50 and approximately 0.18 k cm2, respectively. Within

the reduced model, this local resistance drop would shunt a given synaptic current and reduce the associated voltage response. The model does not directly simulate endplate-current waveforms, junctional-fold geometry, voltage-gated sodium-channel availability, or the neuromuscular safety factor.

For the nominal initial effective conductance gMAC,0=5.0 mS cm-2, a generic reduction at trepair=50 ms representing a repair factor of Rf=0.90 left a residual effective conductance of 0.5 mS cm-2. Under the reduced two-conductance model, the steady voltage shifted from approximately -16.8 mV before repair toward -47.5 mV after repair, and modeled local specific input resistance increased from approximately 0.18 to 1.0 k cm2 (Fig. 2c). This represents partial electrical recovery under the stated model assumptions.

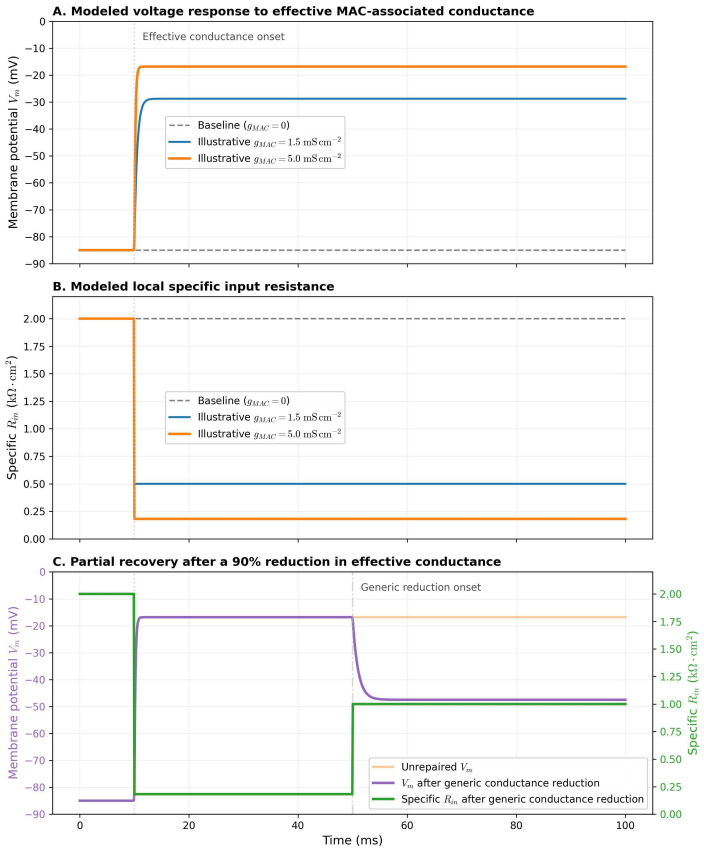


Figure 2: **Illustrative electrical consequences of an effective complement-associated conductance in a reduced postsynaptic membrane model.** (**a**) Numerical voltage trajectories after onset of an effective time-dependent conductance, gMAC, under the nominal assumptions gleak=0.5 mS cm-2, Eleak=-85 mV, and EMAC=-10 mV. Illustrative conductances of 1.5 and 5.0 mS cm-2 produce conductance-weighted steady-state voltages of approximately -28.8 and -16.8 mV, respectively. (**b**) Corresponding modeled local specific input resistance, calculated as Rin,specific=1/(gleak+gMAC). (**c**) A generic repair-factor scenario in which a 90% reduction of an initial 5.0 mS cm-2 effective conductance leaves a residual 0.5 mS cm-2 conductance. The model predicts partial recovery toward approximately -47.5 mV and 1.0 k cm2. Conductances are effective sensitivity variables and are not direct measurements of MAC pore number, conductance density, or lesion kinetics at a human neuromuscular junction.

3.2 Baseline state and analytical verification

Numerical steady-state voltages derived from the RK45 solver were compared with the closed-form solution (Eq. 12). Across 200 values of effective gMAC spanning 0–10 mS cm-2 at fixed EMAC=-10 mV (applied continuously from t=0 to 200 ms), the maximum absolute difference between the numerical voltage at 200 ms and the analytical steady state under nominal tolerances was 2.410-6 mV. The 200 ms evaluation time was much longer than the longest nominal membrane time constant of 2 ms, making residual transient relaxation negligible for this steady-state comparison. Tightening relative and absolute tolerances from 10-3 and 10-5 to 10-6 and 10-8 systematically reduced the integration error while increasing ODE function evaluations as expected (Fig. 3a–c).

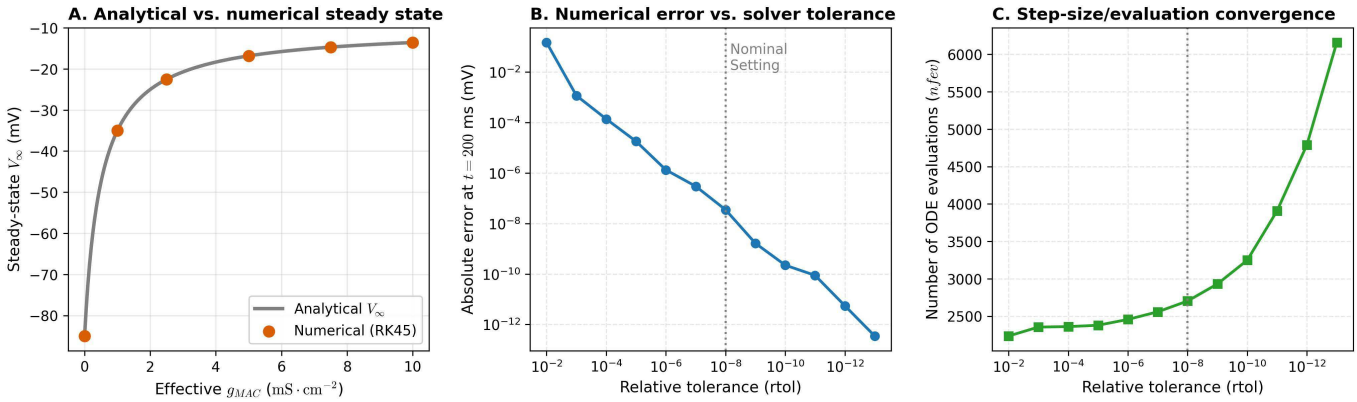


Figure 3: **Analytical and numerical verification.** (**a**) Exact analytical steady-state voltage (V) across gMAC=0–10 mS cm-2, with gleak=0.5 mS cm-2, Eleak=-85 mV, and EMAC=-10 mV, alongside discrete numerical RK45 solutions evaluated at 200 ms. (**b**) Log-scaled numerical error relative to the analytical steady-state solution across prescribed solver tolerances. (**c**) Number of ODE function evaluations as a function of the relative-tolerance setting.

3.3 Sensitivity to effective conductance parameters

The steady-state behavior and time constant were evaluated continuously over the stated sensitivity ranges (gMAC[0,10] mS cm-2 and EMAC[-30,+10] mV; Fig. 4a–d). Changes in effective reversal potential (EMAC) bounded the maximum depolarization

magnitude, while increasing gMAC shortened the membrane time constant and accelerated voltage relaxation.

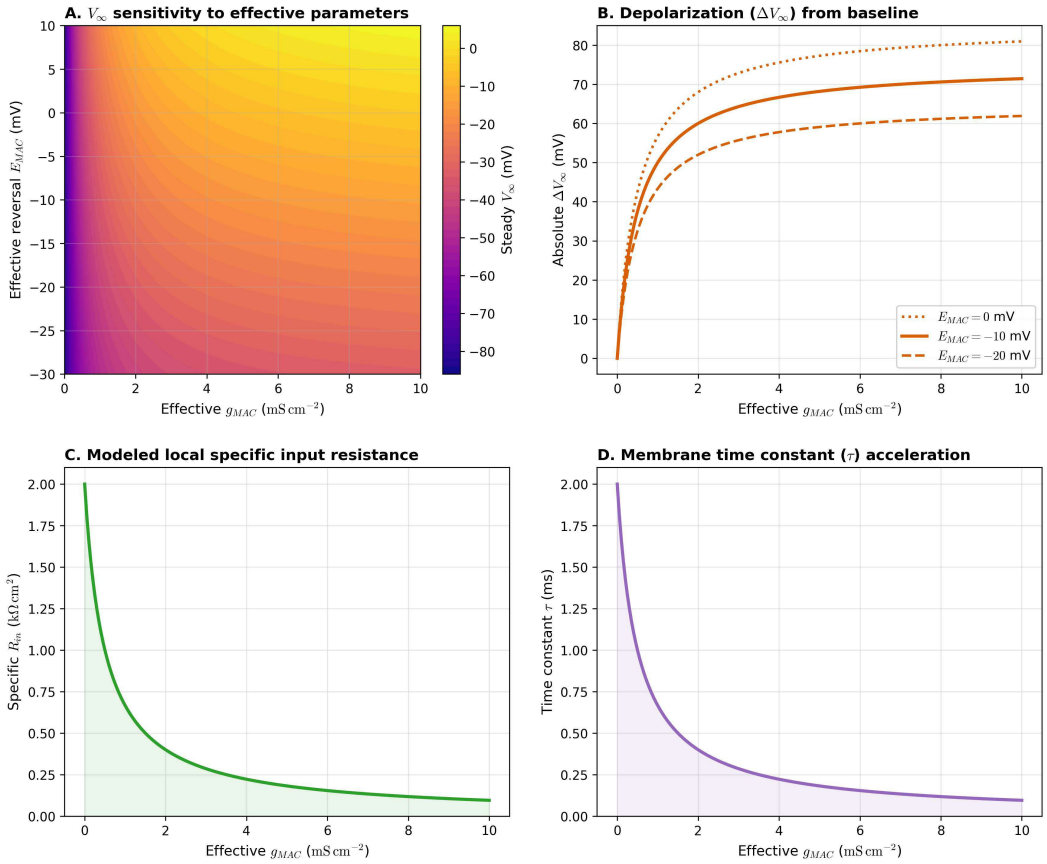


Figure 4: **Steady-state sensitivity to effective conductance and reversal potentials.** (**a**) Conductance-weighted steady state (V) across effective gMAC (0–10 mS cm-2) and EMAC (-30 to +10 mV). (**b**) Magnitude of absolute steady-state depolarization from baseline under bounded reversal assumptions (EMAC=-20,-10,0 mV). (**c**) Modeled local specific input resistance across the evaluated effective-conductance space. (**d**) Calculated shortening of the membrane time constant, plotted as m=cm/(gleak+gMAC).

Shorter transient effective-conductance pulses (Tlesion=0.01–2.0 ms in the analytical contour sweep and 2,10,40 ms in illustrative numerical trajectories) constrained peak depolarization below V, dictated by the RC charging envelope, while the post-repair steady-state voltage and input resistance varied nonlinearly across the (Rf,gMAC,0) parameter grid (Fig. 5a–d).

3.4 Conditional reporter-state sensitivity

The conditional probability of exposing a generic conformational reporter state was evaluated across Vm[-100,+20] mV, F[0.0,3.0], and composite coupling values 0.0,0.02,0.05,0.10 mV-1 at Greporter,0/(kBT)=2.0 (Fig. 6a–d). The specified local-field coupling parameters produced conditional energetic shifts within the evaluated parameter ranges.

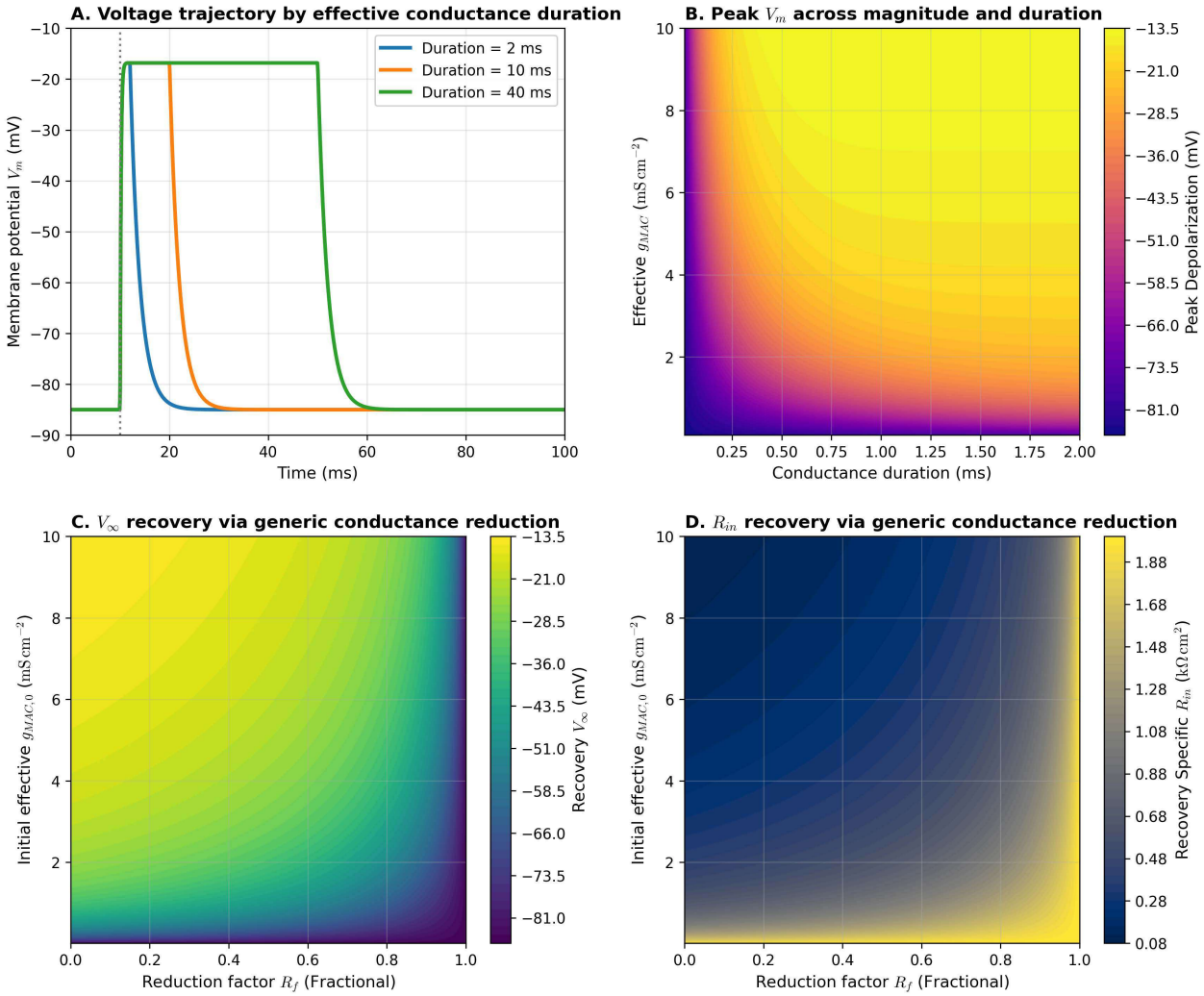


Figure 5: **Dynamic effective conductance and generic reduction sensitivity.** (**a**) Numerical voltage trajectories for variable-duration effective-conductance pulses (Tlesion=2,10,40 ms at gMAC=5.0 mS cm-2). (**b**) Peak depolarization, calculated from the constant-conductance analytical RC charging solution at pulse termination, across conductance magnitude (0.1–10 mS cm-2) and pulse duration (0.01–2.0 ms). (**c**) Post-reduction steady-state V as a function of repair factor Rf (0–1) and initial effective conductance gMAC,0 (0.01–10 mS cm-2), using gMAC=gMAC,0(1-Rf) with gleak, Eleak, and EMAC fixed at their nominal values. (**d**) Post-reduction specific input resistance over the identical parameter grid.

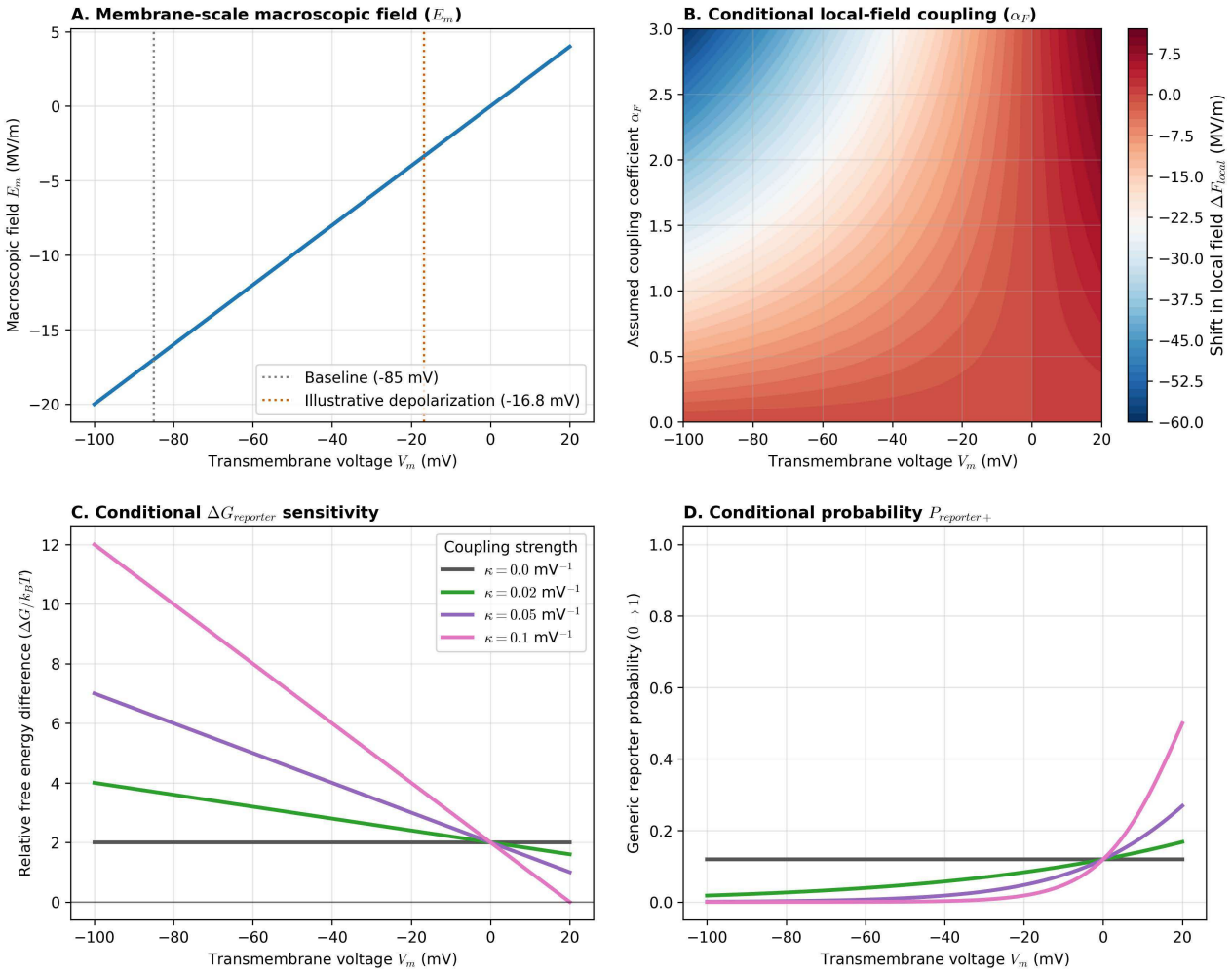


Figure 6: **Conditional generic reporter-state sensitivity analysis.** (**a**) Macroscopic membrane-scale field mapping (Em=Vm/dm) over Vm[-100,+20] mV for dm=5 nm. (**b**) Theoretical local-field shift (Flocal=FVm/dm) derived from conditional F[0.0,3.0] coupling with Vref=0 mV and Findependent=0. (**c**) Conditional sensitivity of the normalized free-energy difference Greporter/(kBT)=2.0-Vm across composite coupling strengths 0.0,0.02,0.05,0.10 mV-1. (**d**) Modeled reporter-positive-state probability Preporter+ across the evaluated voltage and coupling space. This phenomenological parameter-space analysis does not establish a voltage-responsive autoimmune epitope in native AChR, a two-state receptor transition, or altered binding of disease-relevant antibodies.

4 Discussion

Under its stated assumptions, this reduced conductance model predicts that illustrative effective specific conductance scenarios can alter postsynaptic membrane voltage, local specific input resistance, and the model membrane time constant. The model highlights the theoretical importance of localized parallel leak current in complementing established structural mechanisms of AChR injury.

4.1 Integration with structural and synaptic modeling

Advances in structural biology and neurobiology provide an important context for interpreting these reduced-model bounds. Cryo-EM reconstructions of human C5b-9 (Menny et al., 2018) and single-molecule atomic-force microscopy kinetics of MAC assembly (Parsons et al., 2019) demonstrate that the MAC is not a rigid, uniform cylinder, but rather an asymmetric, split-washer -barrel whose incomplete arc intermediates and lipid-disrupting rim regions can permeabilize membranes prior to lytic ring closure. This structural and kinetic heterogeneity supports treating gMAC(t) and EMAC as continuous sensitivity variables rather than fixed multiples of a single planar-bilayer channel prior (Benz et al., 1986).

Similarly, physiological and biophysical analyses of the neuromuscular junction emphasize that synaptic transmission reliability depends on the spatial arrangement of AChRs at the crests of postsynaptic folds and the high input impedance of the narrow fold necks, which amplify local endplate potentials toward the voltage-gated sodium-channel threshold (Wood and Slater, 2001). While spatially resolved multicompartment or finite-element models capture fold geometry and receptor-loss dynamics, our lumped RC formulation isolates a complementary biophysical mechanism: a > 90% reduction in local specific input resistance (Rin,specific dropping from 2.0 to 0.18 k cm2 at gMAC=5.0 mS cm-2) combined with sustained local depolarization toward -16.8 mV. In a spatially resolved endplate, a localized conductive shunt could attenuate the voltage response to AChR-mediated current, while sustained depolarization could reduce perijunctional voltage-gated sodium-channel availability, potentially compounding the functional deficit caused by antibody-mediated AChR internalization and fold simplification (Huijbers et al., 2022). These spatial and active-conductance consequences are not directly evaluated by the present model. Furthermore, high-resolution cryo-EM structures of nicotinic receptors across functional states—such as the human 7 nicotinic receptor (Noviello et al., 2021) alongside computational trans-

membrane domain models of muscle-type AChR (Song and Corry, 2009)—illustrate the atomic-level structural frameworks needed to parameterize future molecular dynamics and Poisson–Boltzmann electrostatic calculations to test the conditional field-coupling coefficient (F) formalized in Eqs. 8–10.

4.2 Model scope and limitations

This framework assumes a lumped electrical compartment and does not resolve fine spatial details of human motor-endplate architecture, nor does it couple directly to neuromuscular transmission kinetics or explicit safety-factor calculations (Wood and Slater, 2001). Poloxamer 188 (P188) is one possible experimental comparator for testing a generic membrane-repair perturbation. Prior studies indicate that P188 can influence membrane stabilization or repair in selected injury models, but these studies do not establish that P188 reduces C5b-9-associated conductance at the neuromuscular junction (Yasuda et al., 2005; Collins et al., 2007; Kwiatkowski et al., 2020). P188 formulations have also been associated with complement activation in human sera, underscoring the need to measure complement products in any proposed experimental comparison (Moghimi et al., 2004). Experimental evaluation should measure effective membrane current, membrane voltage, ionic flux, cell injury, endplate function, and complement activation products using validated assays (Bergseth et al., 2013).

Statements and Declarations

Funding

This research did not receive any specific grant from funding agencies in the public, commercial, or not-for-profit sectors.

Competing Interests

Kevin Thorsen Baird is the Principal Investigator at The C4 Institute, Baird Research & Strategic Sciences, LLC (Fort Myers, FL 33907, USA), and discloses a U.S. provisional patent application (Application No. 64/100,482), assigned to Baird Research & Strategic Sciences, LLC, concerning bioelectric boundary-modulation concepts and computational modeling frameworks related to this work.

Ethics Approval

This study involved theoretical and computational modeling only; no new experiments involving human participants, human tissue, or animals were conducted.

Consent to Participate and Consent for Publication

Not applicable.

Data Availability

All parameter values and analytical equations supporting the findings of this study are reported within the article and Tables 1 and 2. Deterministic numerical simulation outputs and high-resolution figures are publicly archived at https://doi.org/10.13140/RG.2.2.22939.63525.

Code Availability

The Python 3.10 simulation scripts (`numpy`, `scipy`, `matplotlib`) used to integrate the membrane equations and generate Figs. 1–6 are publicly archived at https://doi.org/10.13140/RG.2.2.22939.63525.

Author Contributions

Kevin Thorsen Baird conceived the study, formulated the mathematical model, implemented and verified the numerical simulations, generated the figures, and wrote and revised the manuscript. The author read and approved the final manuscript.

Use of Large Language Models (LLMs)

During preparation of this manuscript, the author used Google Gemini and QuillBot AI for language editing, organizational drafting, formatting support, and software-development suggestions. The author reviewed, tested where applicable, revised, and approved all AI-assisted output, and performed and independently verified the model design, parameter selection, code execution, numerical analyses, figure generation, citation verification, and scientific interpretation.

References

Benz R, Schmid A, Wiedmer T, Sims PJ (1986) Single-channel analysis of the conductance fluctuations induced in lipid bilayer membranes by complement proteins C5b-9. J Membr Biol 94:37–45. https://doi.org/10.1007/BF01901011

Bergseth G, Ludviksen JK, Kirschfink M, Giclas PC, Nilsson B, Mollnes TE (2013) An international serum standard for application in assays to detect human complement activation products. Mol Immunol 56:232–239. https://doi.org/10.1016/j.molimm.2013.05.221

Collins JM, Despa F, Lee RC (2007) Structural and functional recovery of electropermeabilized skeletal muscle in vivo after treatment with surfactant Poloxamer 188. Biochim Biophys Acta Biomembr 1768:1238–1246. https://doi.org/10.1016/j.bbamem.2007.01.012

Fried SD, Boxer SG (2015) Measuring electric fields and noncovalent interactions using the Vibrational Stark Effect. Acc Chem Res 48:998–1006. https://doi.org/10.1021/acs.accounts.5b00035

Gilhus NE (2016) Myasthenia gravis. N Engl J Med 375:2570–2581. https://doi.org/10.1056/NEJMra1602678

Howard JF Jr (2018) Myasthenia gravis: The role of complement at the neuromuscular junction. Ann N Y Acad Sci 1412:113–128. https://doi.org/10.1111/nyas.13522

Howard JF Jr, Utsugisawa K, Benatar M, Murai H, Barohn RJ, Illa I, Jacobus S, Vissing J, Burns TM, Guptill JT et al (2017) Safety and efficacy of eculizumab in anti-acetylcholine receptor antibody-positive refractory generalised myasthenia gravis (REGAIN): A phase 3, randomised, double-blind, placebo-controlled, multicentre study. Lancet Neurol 16:976–986. https://doi.org/10.1016/S1474-4422(17)30369-1

Huijbers MG, Marx A, Plomp JJ, Le Panse RL (2022) Advances in the understanding of disease mechanisms of autoimmune neuromuscular junction disorders. Lancet Neurol 21:163–175. https://doi.org/10.1016/S1474-4422(21)00357-4

Kwiatkowski TA, Rose AL, Jung R, Capati A, Hallak D, Yan R, Weisleder N (2020) Multiple poloxamers increase plasma membrane repair capacity in muscle and nonmuscle

cells. Am J Physiol Cell Physiol 318:C253–C262. https://doi.org/10.1152/ajpcell.00321.2019

Menny A, Serna M, Boyd CM, Gardner S, Joseph AP, Morgan BP, Topf M, Brooks NJ, Bubeck D (2018) CryoEM reveals how the complement membrane attack complex ruptures lipid bilayers. Nat Commun 9:5316. https://doi.org/10.1038/s41467-018-07653-5

Moghimi SM, Hunter AC, Dadswell CM, Savay S, Alving CR, Szebeni J (2004) Causative factors behind Poloxamer 188 (Pluronic F68, Flocor)-induced complement activation in human sera. Biochim Biophys Acta Mol Basis Dis 1689:103–113. https://doi.org/10.1016/j.bbadis.2004.02.005

Morgan BP (1989) Complement membrane attack on nucleated cells: Resistance, recovery and non-lethal effects. Biochem J 264:1–14. https://doi.org/10.1042/bj2640001

Mozrzymas JW, Lorenzon P, Riviera AP, Tedesco F, Ruzzier F (1993) An electrophysiological study of the effects of myasthenia gravis sera and complement on rat isolated muscle fibres. J Neuroimmunol 45:155–162. https://doi.org/10.1016/0165-5728(93)90176-Y

Noviello CM, Gharpure A, Mukhtasimova N, Cabuco R, Baxter L, Borek D, Sine SM, Hibbs RE (2021) Structure and gating mechanism of the 7 nicotinic acetylcholine receptor. Cell 184:2121–2134.e13. https://doi.org/10.1016/j.cell.2021.02.049

Okamoto K, Wang W, Rounds J, Chambers E, Jacobs DO (2000) Sublytic complement attack increases intracellular sodium in rat skeletal muscle. J Surg Res 90:174–182. https://doi.org/10.1006/jsre.2000.5880

Parsons ES, Stanley GJ, Pyne ALB, Hodel AW, Nievergelt AP, Menny A, Yon AR, Rowley A, Richter RP, Fantner GE, Bubeck D, Hoogenboom BW (2019) Single-molecule kinetics of pore assembly by the membrane attack complex. Nat Commun 10:2066. https://doi.org/10.1038/s41467-019-10058-7

Sahashi K, Engel AG, Lambert EH, Howard FM Jr (1980) Ultrastructural localization of the terminal and lytic ninth complement component (C9) at the motor end-plate in myasthenia gravis. J Neuropathol Exp Neurol 39:160–172. https://doi.org/10.1097/00005072-198003000-00005

Song C, Corry B (2009) Computational study of the transmembrane domain of the acetylcholine receptor. Eur Biophys J 38:961–970. https://doi.org/10.1007/s00249-009-0476-3

Vu T, Meisel A, Mantegazza R, Annane D, Katsuno M, Aguzzi R, Enayetallah A, Beasley KN, Rupp J, Howard JF Jr et al (2022) Terminal complement inhibitor ravulizumab in generalized myasthenia gravis. NEJM Evid 1:EVIDoa2100066. https://doi.org/10.1056/EVIDoa2100066

Wood SJ, Slater CR (2001) Safety factor at the neuromuscular junction. Prog Neurobiol 64:393–429. https://doi.org/10.1016/S0301-0082(00)00055-1

Yasuda S, Townsend D, Michele DE, Favre EG, Day SM, Metzger JM (2005) Dystrophic heart failure blocked by membrane sealant poloxamer. Nature 436:1025–1029. https://doi.org/10.1038/nature03844